
HYPERSPPECTRAL IMAGE RESTORATION AND SUPER-RESOLUTION WITH PHYSICS-AWARE DEEP LEARNING FOR BIOMEDICAL APPLICATIONS

A PREPRINT

Yuchen Xiang^{*,1} yuchen.xiang@imperial.ac.uk	Zhaolu Liu^{*,2} zhaolu.liu16@imperial.ac.uk	Monica Emili Garcia-Segura^{1,4} me485@cam.ac.uk
Daniel Simon¹ d.simon19@imperial.ac.uk	Boxuan Cao¹ caoboxuan1998@gmail.com	Vincen Wu¹ vwu@ethz.ch
Kenneth Robinson¹ k.robinson@imperial.ac.uk	Yu Wang³ yu.wang1@imperial.ac.uk	Ronan Battle³ ronan.battle15@imperial.ac.uk
Robert T. Murray³ robert.murray10@imperial.ac.uk	Xavier Altafaj⁵ xaltafaj@ub.edu	Luca Peruzzotti-Jametti^{1,4} lp429@cam.ac.uk
Zoltan Takats¹ z.takats@imperial.ac.uk		

1. Department of Metabolism, Digestion and Reproduction, Imperial College London, London, UK
 2. Department of Mathematics, Imperial College London, London, UK
 3. Department of Physics, Imperial College London, London, UK
 4. Department of Clinical Neurosciences and NIHR Biomedical Research Centre, University of Cambridge, Cambridge, UK
 5. Department of Biomedicine, University of Barcelona, Barcelona, Spain
- *these authors contributed equally to the manuscript.

ABSTRACT

Hyperspectral imaging is a powerful bioimaging tool which can uncover novel insights, thanks to its sensitivity to the intrinsic properties of materials. However, this enhanced contrast comes at the cost of system complexity, constrained by an inherent trade-off between spatial resolution, spectral resolution, and imaging speed. To overcome this limitation, we present a deep learning-based approach that restores and enhances pixel resolution post-acquisition without any *a priori* knowledge. Fine-tuned using metrics aligned with the imaging model, our physics-aware method achieves a $16\times$ pixel super-resolution enhancement and a $12\times$ imaging speedup without the need of additional training data for transfer learning. Applied to both synthetic and experimental data from five different sample types, we demonstrate that the model preserves biological integrity, ensuring no features are lost or hallucinated. We also concretely demonstrate the model's ability to reveal disease-associated metabolic changes in Down's syndrome that would otherwise remain undetectable. Furthermore, we provide physical insights into the model's inner workings, paving the way for future refinements that could potentially surpass instrumental limits in an explainable manner. All methods are available as open-source software on GitHub (<https://github.com/oycxyd/HyReS>).

Keywords hyperspectral imaging, mass spectrometry imaging, super-resolution, physics-aware deep learning, explainable AI

1 Introduction

Hyperspectral imaging (HSI) is a powerful tool for biomedical applications, where the spectral properties of different biological substances can vary significantly. For instance, differences between diseased and healthy tissues can be easily identified, leading to the development and implementation of clinically approved diagnostic and surgical tools Fabelo et al. [2018], Yoon [2022]. In recent years, novel avenues of spectral analysis have been explored, yielding high-contrast images for applications that require biophysical, mechanical, and chemical information Singh et al. [2020], Kabakova et al. [2024], Jones et al. [2019]. These unique mechanisms reveal details that are otherwise invisible with conventional imaging modalities.

Mass Spectrometry Imaging (MSI) is one such HSI technique that has seen significant advances over the last decade because of its unparalleled ability to multiplex thousands of chemical species in a single spectrum and provide their respective spatial mappings. Since its inception in the 1960s, modern MSI can now operate under ambient conditions with minimal or no sample preparation Wiseman et al. [2006], Simon et al. [2023], making it indispensable in fields such as cancer research, neuroscience, and pharmaceutical research Xiao et al. [2020]. Despite promising results,

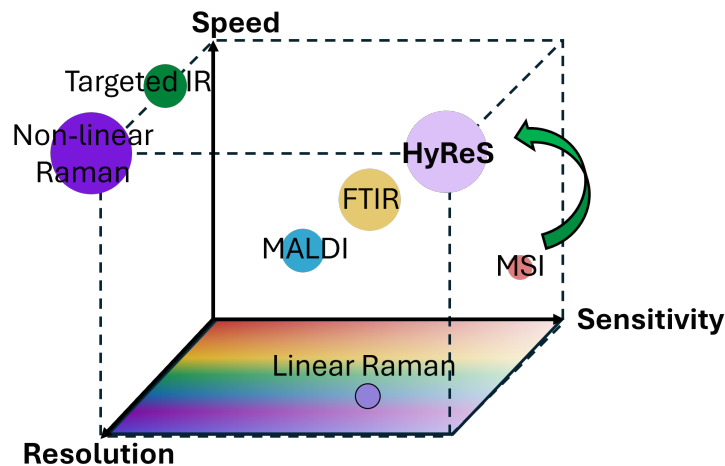


Figure 1: *The 3S space limiting hyperspectral imaging in general and competitor analysis of major approaches granting chemical contrast comparable to that of MSI, with respect to the proposed DL-SISR scheme.*

the widespread adoption of HSI in biomedicine has been limited. This is primarily due to the well-documented trade-offs between spectral resolution, spatial resolution, and imaging speed (the "3S" triangle), which pose significant challenges, especially in applications requiring fast, real-time operation. Hardware solutions such as spectral scanning and encoding Abdo et al. [2019] have led to further optimization, but they still cannot overcome the inherent limitations imposed by the 3S triangle (Fig. 1). Similarly, MSI is constrained by the same triangular limitations. Although MSI generally excels in spectral resolution due to the high sampling rates of common mass spectrometers, its spatial resolution typically falls within the $10\ \mu\text{m}$ – $100\ \mu\text{m}$ range Xue et al. [2019], Wu et al. [2022], which is significantly lower than that of optical imaging techniques. Achieving higher spatial resolution often comes at the expense of imaging speed. This limitation in spatial resolution may hinder the interpretability of MSI data when combined with currently accepted standards, such as bright-field optical imaging. To address these challenges, existing solutions have often employed image fusion approaches Van de Plas et al. [2015], Hu and Laskin [2022] to "guide" the localisation of important features. However, these methods are not universally applicable and typically require some level of prior knowledge before fusion can be performed.

To address the intrinsic challenges of HSI, we propose a purely software-based solution in the form of deep learning-facilitated single image super-resolution (DL-SISR). While there is significant interest in DL-SISR within the field of computer vision, particularly for natural scenery images Huang et al. [2022], Ledig et al. [2016], existing state-of-the-art models typically rely on perceptual metrics-based learning Wang et al. [2019, 2021] that focus on pixelwise differences, without incorporating the underlying physical principles of the imaging process. This makes them less suitable for bioimaging using HSI, where the preservation of spectral and spatial integrity is crucial. Although recent work has implemented DL-SISR algorithms for microscopy Weigert et al. [2018], these models primarily enhance perceptual quality rather than achieving true sub-diffraction limit super-resolution Qiao et al. [2021]. This limitation arises in part from the fundamentally ill-posed nature of the SISR problem, which involves finding a one-to-many mapping from

low-resolution (LR) to high-resolution (HR) images. Consequently, there is a high demand for representative training data, which can be challenging to obtain in bioimaging. In contrast, our approach does not need additional training data apart from the data to be restored by introducing a physics-informed model that imposes physically meaningful constraints in the Fourier domain to regularise the training process. By incorporating these constraints, our model goes beyond mere perceptual quality improvement, as this physics-based approach helps ensure that the reconstructed images are not only visually accurate but also faithful to the underlying physical properties of the HSI system.

We demonstrate our custom-designed, end-to-end workflow, which facilitates Deep Learning-based Hyperspectral Image Restoration and Super-resolution (HyReS), optimised specifically for HSI. Through various simulated and experimental cases, we show that HyReS functions as an "all-in-one" toolbox capable of both resolution restoration and pixel super-resolution post-acquisition of HSI data, effectively surpassing the hardware limitations of current HSI technology while maintaining information fidelity for downstream analyses. Crucially, HyReS provides valuable physical insight into whether "true" super-resolution can be achieved, potentially enabling the restoration of novel features that were not discernible in the low-resolution data.

2 Results

2.1 Image restoration of synthetic data

We first explore the use of HyReS to restore undersampled images, as a major interest of applying DL-SISR for HSI is to leverage the speed-up achieved through recovering high-resolution details from low-resolution input taken within a fraction of the time required. To-date, robust quality improvement along upsampling has already been observed, as we Xiang et al. [2023] and others Liao et al. [2023] have reported on transfer learning approaches with state-of-the-art (SOTA) models Wang et al. [2019], Weigert et al. [2018]. Different to other approaches that require well-curated image pairs between different modalities, we present a solution to generate naturally paired training data by synthetically downsampling with the consideration of detector noise (4.5). As well as the perceptual quality of the restoration, understanding the effect of such approaches on downstream analyses is also crucial for applications such as digital pathology, where objective and trustworthy assessment is key. To explore such a scenario, we trained a HyReS model with our unique Fourier Ring Correlation-based generative adversarial networks (FRCGAN) based on MSI images of human breast biopsies that have corresponding hematoxylin-eosin (H&E) stained optical images and histopathology assessment. The input images were sampled with $50\ \mu\text{m}$ pixel size and their LR counterparts needed for training are synthetically generated by downsampling bicubically in this case to resemble those sampled with $200\ \mu\text{m}$ pixels. The trained model was then used to perform 4-times upsampling with the LR images as input. To simulate a pathology task, segmentation analysis was performed on both the original HR and HyReS-restored images to facilitate digital 'staining' of the tissue into distinct regions of pathological interest. The segmentation was achieved using a mainstream approach that utilises dimension reduction by UMAP McInnes et al. [2018] and subsequent clustering by HDBSCAN Ester et al. [1996], the parameters were kept identical for both sets of images (4.6). Compared to the H&E-stained reference (Figure 2), it can be seen that both the original and restored data give enhanced contrast in segmenting the tumourous (red) and healthy regions on tissue, thanks to the rich spectral information. The latter can be further identified to be either fatty or muscular areas, indicated by the blue and green segments respectively (Figure 2b), agreeing well with the pre-assessment performed on the H&E data. To numerically evaluate the effect of HyReS on segmentation analysis, we compute the Sørensen-Dice similarity coefficient between the two segmented images, from which an average score of 0.6701 was obtained. While the overall segmentation appears largely similar, the main quantitative difference originates from the muscular and fatty regions. More homogeneous clusters are visibly formed using restored data both in terms of visual perception of the image and their distributions in UMAP space (Figure 2a). Cluster tearing is more obvious in the original data and as such a significant number of data points remain unclustered, which are both respective issues with the UMAP and HDBSCAN algorithms that are well-documented. While the segmentation approach can be optimised parametrically to suit the data, in an unbiased comparison the HyReS-restored data therefore appear more resilient to algorithmic particularity and improves the analysis.

2.2 Image restoration of experimental data

Encouraged by the restoration power of HyReS on synthetic data, we further investigate if it can be used to restore experimental data with the main motivation of improving imaging speed without compromising resolution. Both HR ($25\ \mu\text{m}$ pixel resolution) and LR images ($100\ \mu\text{m}$ pixel resolution) on adjacent mouse brain sections were acquired to serve as the training and test data respectively. After training a FRCGAN model on the HR data, the LR images were used as input to demonstrate the restoration effect. A summary of the results is visualised in Figure 3 by means of pseudo-RGB images comprising three representative spectral channels with discernible brain morphology. Apart from clearly enhancing the resolution of the LR inputs, the HyReS-restored output images were also observed to have

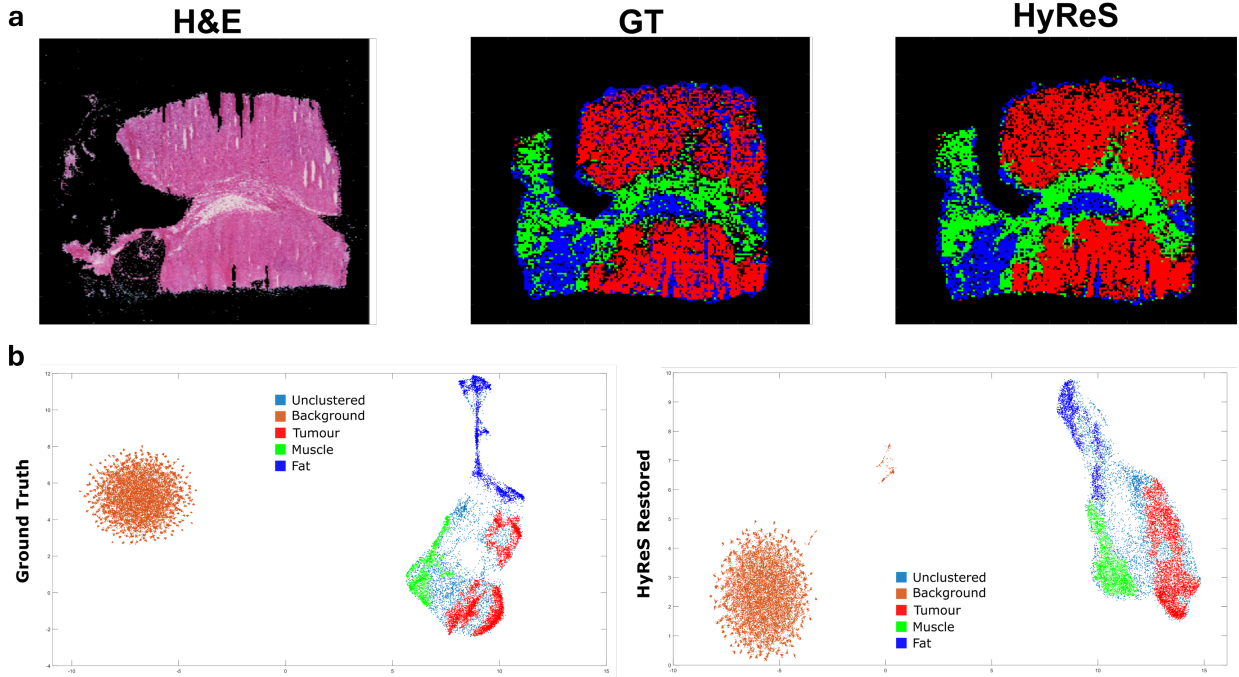


Figure 2: Restoration of synthetically downsampled breast biopsy images and effect on segmentation. a) Comparison of image segmentation results from both the ground truth (GT) images and those that have been restored by HyReS after downsampling. The optical image of an adjacent tissue that has been H&E-stained is also shown, whose pathological annotations also provided tentative assignment of the segmented regions. Namely, Red = Tumour, Green = Muscle, Blue = Fat. b) Comparison of the clustering and hence image segmentation behaviour for both the GT and HyReS-restored data in a dimensionally reduced 2D domain provided by UMAP. The pathological annotations are illustrated in the same colours as in a).

visibly improved SNR and quality when pitched against the HR ‘ground truth’ (Fig. 3). This reflects directly on the robustness of our approach and its applicability to some MSI-specific properties, for instance the counter-intuitive decrease in SNR and higher possibility of artefact production in HR imaging data due to material removal Metodiev et al. [2021] and longer imaging time. To quantitatively illustrate this enhancement effect, both the CRISQUE scores and FRC-calculated resolutions are compared for the top 300 highest intensity images in each group. In accordance with the qualitative observation, the image quality increases sequentially going from the LR input to the HyReS output, giving median scores of 43.23, 44.04 and 46.88 respectively. Conversely, the estimated resolutions see a dramatic enhancement from the average of $531.4\ \mu\text{m}$ in the input dataset to $87.2\ \mu\text{m}$ in the restored dataset, with a much tighter distribution, indicating a ubiquitous effect on most input images. In contrast, the GT HR dataset possesses an average resolution of only $212.5\ \mu\text{m}$, instead of the expectation that it should be four-fold superior to the LR. This can be attributed to the decreased SNR levels and hence lower frequency cut-off points when physically imaging in HR and further strengthens our motivation of a software-based approach to higher resolution.

In terms of imaging speed, the HR data was acquired at a rate of 100 ms/pixel with a total of 207680 pixels, equating to a total run time of around 6 hours. In contrast, at the same sampling rate the LR data only took around 30 minutes and the HyReS restoration an additional 3 minutes. This approach thus represents an order of magnitude effective time save to current hardware-limited MSI without loss of resolution and we believe this to be an exciting new avenue for achieving high-speed imaging in applications where throughput is a major incentive, e.g., digital pathology.

2.3 Classification of multiple sclerosis lesions using HyReS-restored images

On the back of excellent restoration performance by applying HyReS, we further investigated whether the HyReS-restored images can preserve the information of original images in a biological context, for which we need a ‘ground truth’ dataset with known biological implications. We have previously reported on the ability of ambient MSI to metabolically profile experimental autoimmune encephalomyelitis (EAE) mouse models *in situ* in the scope of multiple sclerosis (MS). MS is a chronic autoimmune disorder of the central nervous system (CNS) that affects millions of

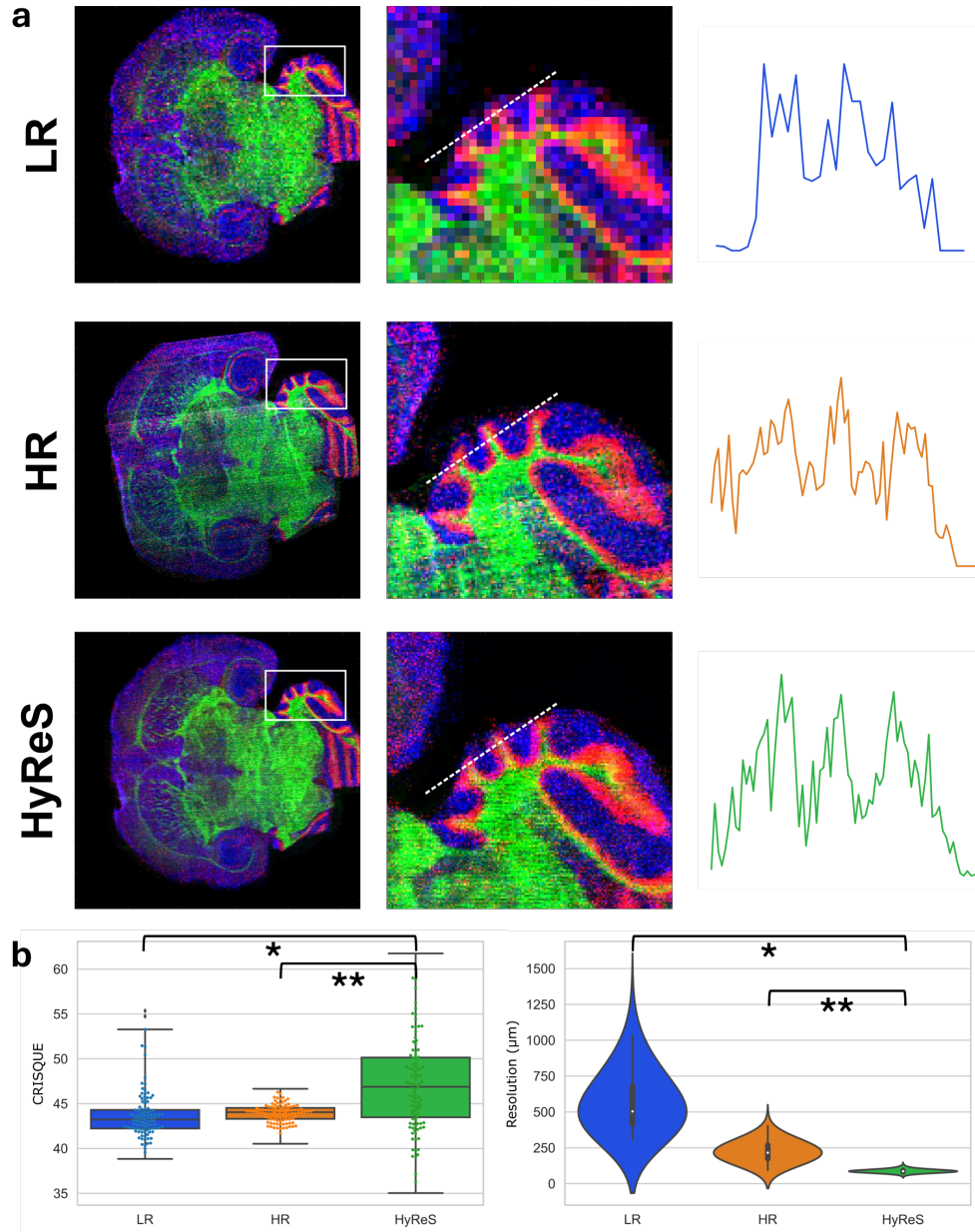


Figure 3: *a*) Comparison of RGB ion images (Red:m/z 150.0 Green:m/z 600.5 Blue:m/z 864.6) of mouse brains that have been acquired at low resolution (LR) with 100 μm pixels, at high resolution (HR) with 25 μm pixels and when restored to HR from LR by HyReS. A linescan of the pixel intensities along the cerebellum is also shown in each case to depict the relative SNR. *b*) Image quality evaluation of bicubically downsampled (LR), ground truth high resolution (HR) and HyReS-upsampled images using CRSIQUE scores and estimated resolutions.

individuals worldwide. It is characterized by a wide range of neurological symptoms resulting from the immune system's attack on the myelin sheath, ranging from fatigue, muscle weakness to vision impairment Peruzzotti-Jametti et al. [2021]. While the exact cause of MS is still unclear, it is thought to derive from complex interactions of multi-source factors of genetic, environmental, and immunological origins. Additionally, patients with more progressive forms manifest changes in their neuronal metabolism and mitochondrial function.

We have thus investigated and observed stark alterations in the metabolic profiles of spinal chords in our induced EAE model. A comparison of spinal cord sections from healthy control (HC) mice and those at the peak of disease (PD, defined as tissue collected three days after the onset of clinical symptoms) demonstrated a clear difference in the

intensity distributions of various key metabolites Peruzzotti-Jametti et al. [2024]. These features were subsequently used to perform predictive modelling with near perfect accuracy scores and serve as an ideal reference to test the biological generalisability of our approach. To evaluate the effect of HyReS on retaining biological information, the EAE dataset was first downsampled and noise-corrupted accordingly and the same model trained on Down Syndrome data from Section 2.4 was directly applied on the new data to predict their upsampled & denoised counterparts. The same predictive modelling approach was also used to construct classification models based on the downsampled (LR) and restored images respectively using the known features obtained from the ground truth HR images-based model. It

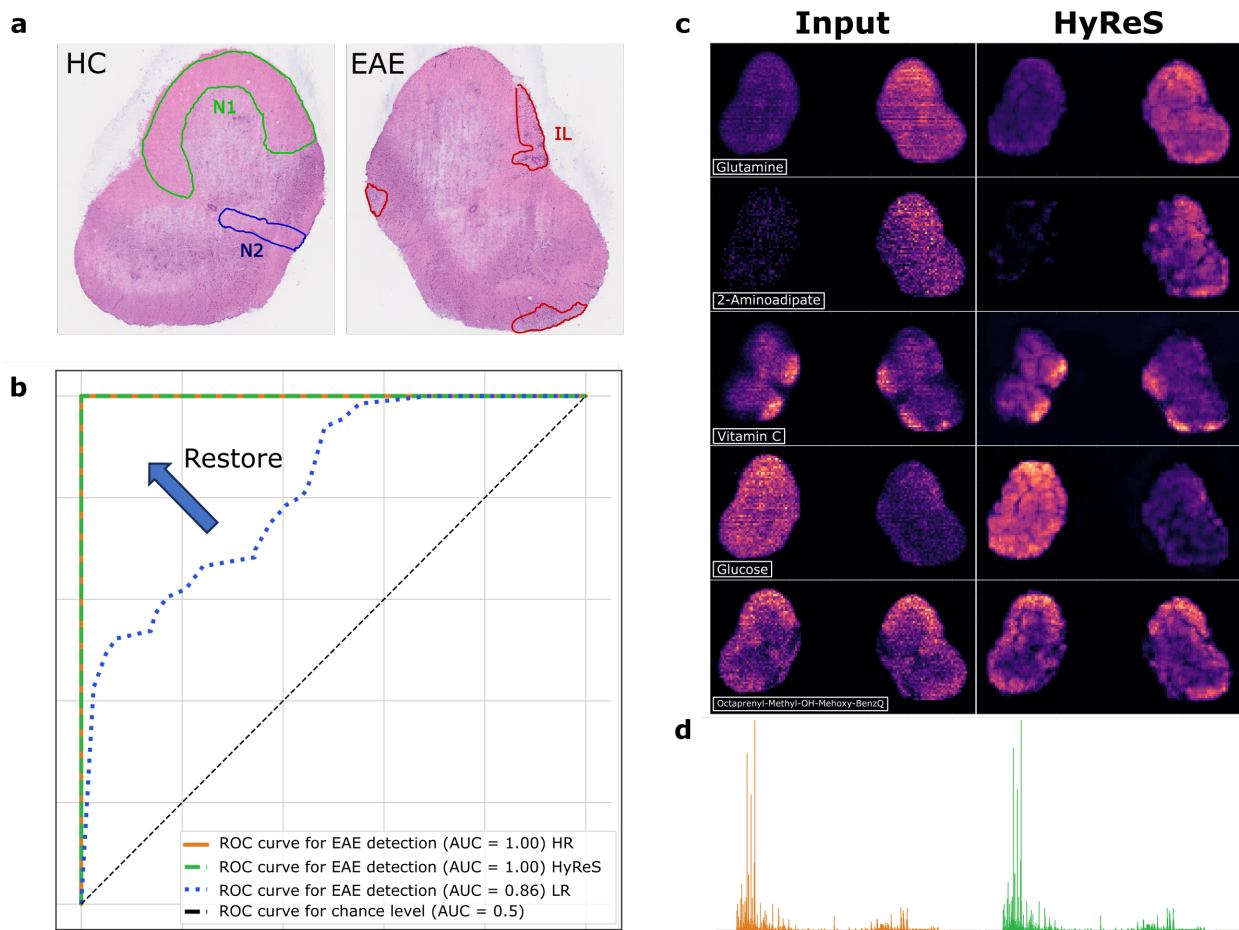


Figure 4: a) H&E stained image from an adjacent slide showing regions-of-interest used of predictive modelling, containing areas of AL/DS/Lesion. b) Predictive modelling results. c) Ion images of key metabolites driving the ground truth classification model before & after HyReS restoration. d) Mean spectra in the spatial metabolomic data before & after HyReS restoration.

is well-documented that machine learning models perform optimally when applied to data comparable to those used in training. While we do not foresee there to be a universal model that can be ubiquitously applied to any new data, we also highlight that the pre-trained FRCGAN still yields high performance in terms of the downstream classification task and does not change the biological conclusion of the study. This is clearly evidenced by the receiver operator characteristics (ROC) curves (Figure 4b), summarising the classification performance on detecting EAE tissue from HC ones. A sharp decrease of $\sim 15\%$ was induced by artificial downsampling, which was subsequently nearly completely restored by a HyReS model that has not seen this data before. This observation can be made for all other classes and their respective metrics are collated in the [Supplementary Materials]. Similarly, visual assessment of images of some significant metabolites previously discovered to be driving the classification also show little to no undesirable restoration effect in the results (Figure 4c), while benefiting from some denoising/-artifacting. Some hallucination effect (i.e. addition of new spatial features from the previous training data that are not present in reality) can be potentially identified when comparing with the optical image of an adjacent slide (Figure 4a), though they evidently do not have a

major impact on any corresponding image analysis. This is further supported by comparing the spectral characteristics of the original and restored datasets (Figure 4d), as their mean spectra were considered to be identical (Figure 4d) according to a Spearman correlation score of 0.9982.

2.4 Image upsampling for enhanced detection of metabolic phenotypes in a Down syndrome murine model

In addition to accelerating imaging speed, HyReS can also be used to enhance biological information that is otherwise difficult to retrieve for common downstream analyses, such as classification. Down’s Syndrome (DS) is a one of the most common genetic disorders worldwide, which is hallmarked by an excess copy of chromosome 21, hence its alternative name of Trisomy 21. Despite significant progress being made in terms of the genetic understanding that directly leads to observable conditions Rachidi and Lopes [2007], deeper insight is still required to decipher the mechanisms that cause the diverse symptoms of DS, which can be physical, intellectual and behavioural. Recent hypothesis has considered treating DS as a “metabolic disease” Dierssen et al. [2020], opening new avenues of metabolic targets that could contribute to understanding pathogenesis, early diagnosis and potential therapeutics. MSI thus provides a unique tool to verify this hypothesis and spatially study the brain metabolic profiles of the Ts65Dn mouse, a trisomic mouse model recapitulating DS-like neuronal, circuitry and behavioural phenotypes Rueda et al. [2012]. To investigate the metabolic interplay of DS and differences between trisomic mice (Ts65Dn, DS mouse model) and disomic (wildtype) littermates in the first study of its kind, we show that HyReS can be used to elucidate this information from hyperspectral images of mouse brains.

To facilitate a statistically relevant study, a total of $n = 20$ mouse brains were sectioned and imaged at a relatively coarse pixel size of $75 \mu\text{m}$ in the interest of imaging speed, which will then be restored 4-fold in both dimensions by HyReS post-acquisition. To test the sensitivity of the resultant data to trisomy, similarly sized regions-of-interest (ROIs) from the cerebral cortices in these brain images were taken to train machine learning models. These models were subsequently optimised via feature refinement (4.3) and then used to predict the aneuploidy-dependent effect of every pixel in the training images ($n = 16$) and also independent test images ($n = 4$).

As a result, two binary classification models were trained on the low-resolution ‘ground truth’ (GT) images directly from the experiment and the corresponding high-resolution HyReS-enhanced images respectively, whose performance was evaluated in Table 1. When cross-validated during optimisation, the HyReS-enhanced model notably selects a total of 317 metabolic features deemed to play a significant role in stratifying trisomic and disomic data. This is 180 more than that attained from the GT model, which leads to an apparent 10% increase in model performance. This performance enhancement is further translated to tissue-based classification when the trained models were applied on whole tissues to predict other pixels that were not seen during training. Namely, the HyReS model robustly achieves an overall accuracy of 82% (13/16 tissues) while the GT model falls sharply to 63% (10/16 tissues), suggesting some level of overfitting with the information available. Finally, when given independent classification tasks, the HyReS model retains superior performance at 83%, only misclassifying one out of four tissues, whereas the GT model is rendered as good as a random coin toss. The quantified assessment of relative performance is also summarised by ROC analysis (Fig. 5a).

While the predictive modelling performance serves as a fair comparison, it does not directly reflect the metabolic information of interest, nor biological consideration such as the fact that any disease-associated abnormalities are not necessarily found in the entire brain. In which case, it is more insightful to interpret the spatial and spectral features involved in classification. To visualise the prediction spatially, the probabilities of pixels being predicted to be trisomic were mapped and overlaid with an image from a channel (m/z 885.54 PI(38:4)) is the MSI dataset that represents the anatomy well. Figure 5b&c demonstrate such overlays of HyReS-enhanced images where the brains from trisomic mice can be clearly distinguished from those from disomic mice due to higher prediction probabilities both in value and in density. Furthermore, despite training the model on pixels from the cerebral cortex alone, the prediction shows localised ‘hot spots’ that are anatomically specific across the brain, highlighting e.g., the dorsal striatum, basal forebrain, and cerebellum. This is in line with expectation as these components play roles in both physical and cognitive functions, which are directly affected by trisomy 21 Dierssen et al. [2020]. More interestingly, the housing arrangement of the experimental mice may also introduce a social element that is further revealed by HyReS, as some trisomic and disomic mice were caged together for the purpose of a behavioural study before the imaging experiment. This arrangement was also reflected in the prediction results, as disomic mice that lived alongside the trisomic ones appeared to be more prone to misclassification. In fact, all of the misclassified cases arising from the HyReS models were from co-caged disomic mice, predicted to have a relatively higher concentration of ‘trisomic pixels’. Specifically, there seemed to be a high localisation in the dorsal striatum, which has also been linked to habit formation Goodman and Packard [2018].

Spectrally, HyReS provides a list of significant features that facilitates further interpretation which may provide biological insight. Even without the exact identification of chemical species, functional interpretation is already possible through algorithms such as mummichog Li et al. [2013], which statistically predicts the activity of metabolic pathways

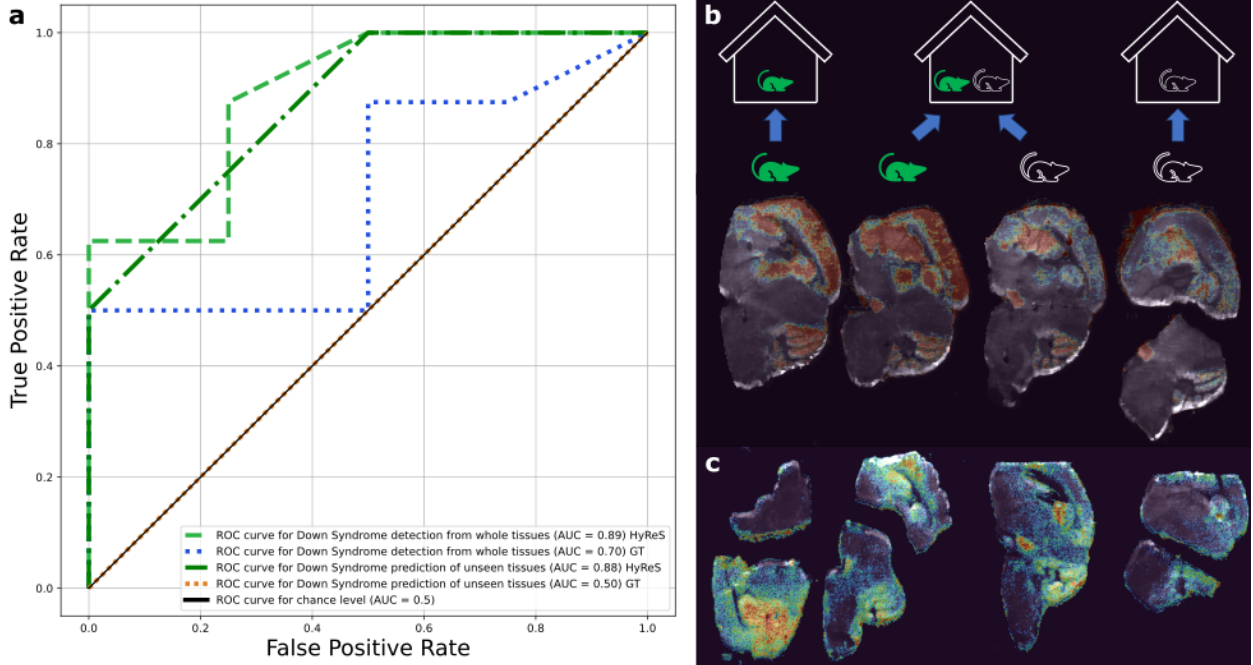


Figure 5: *a) ROC curves summarising the predictive modelling performance of trained models generated from GT and HyReS-enhanced images when applied to validation and independent classification tasks. b) Representative overlay images showing the spatial distribution and intensity of regions predicted to be trisomic when applying the HyReS-enhanced model on whole brain images used for training. The DS status and caging arrangement of the mice before imaging are also indicated, where green corresponds to a trisomic transgenic mouse, and white a normal mouse. c) Overlay images illustrating trisomic prediction when applying the HyReS-enhanced model on independent whole brain images. The same DS status and caging arrangement from b) also apply.*

and networks in play. Figure 6 thus shows the result of such functional analysis which highlights intensity variations that may implicate e.g., Lysine degradation, Valine, Leucine, and Isoleucine biosynthesis and degradation, Glyoxylate and Dicarboxylate metabolism, Tyrosine metabolism, Phenylalanine metabolism and the Citrate cycle. Despite the spuriously high p-values that are due to a limited degree of identification (217 hits from 62 masses), these findings are consistent with previous work. Namely, a recent study by Cai et al. [2023] revealed very similar pathways in mice with Down’s Syndrome, which also affected their social behaviour. In features that have been identified to be significantly up- or down-regulated, potentially identifiable amino acid species are also in line with the trends observed previously in human subjects Caracausi et al. [2018], while heavier lipid species reflect trends that have been linked to comorbidities of DS Worley et al. [2023].

Table 1: *Performance comparison of Down Syndrome detection with models trained on regions from the cerebral cortices of the original and HyReS-enhanced images.*

	Sensitivity	Specificity	Balanced Accuracy	AUC
GT (10-fold CV, 127 features)	0.80	0.80	0.80	0.80
HyReS (10-fold CV, 317 features)	0.90	0.90	0.90	0.90
GT (whole tissue prediction)	0.60	0.67	0.63	0.70
HyReS (whole tissue prediction)	0.85	0.78	0.82	0.89
GT (independent prediction,)	0.50	0.50	0.50	0.50
HyReS (independent prediction)	1.00	0.67	0.83	0.88

In summary, HyReS enhances the spatial and spectral sensitivity for downstream analyses, achieving better results in binary classification than that was obtainable in the original dataset. The spectral improvement can be directly linked to the denoising effect of HyReS which in turn resolves the more subtle intensity differences. In terms of the spatial resolution, HyReS appears to offer more than just denoised, upsampled training data. The restored images have higher spatial frequency cut-offs and higher visual quality scores overall ([Supplementary]), which seems to suggest an enrichment, rather than linear increase in spatial information. While the spatial features in this case are of an anatomical

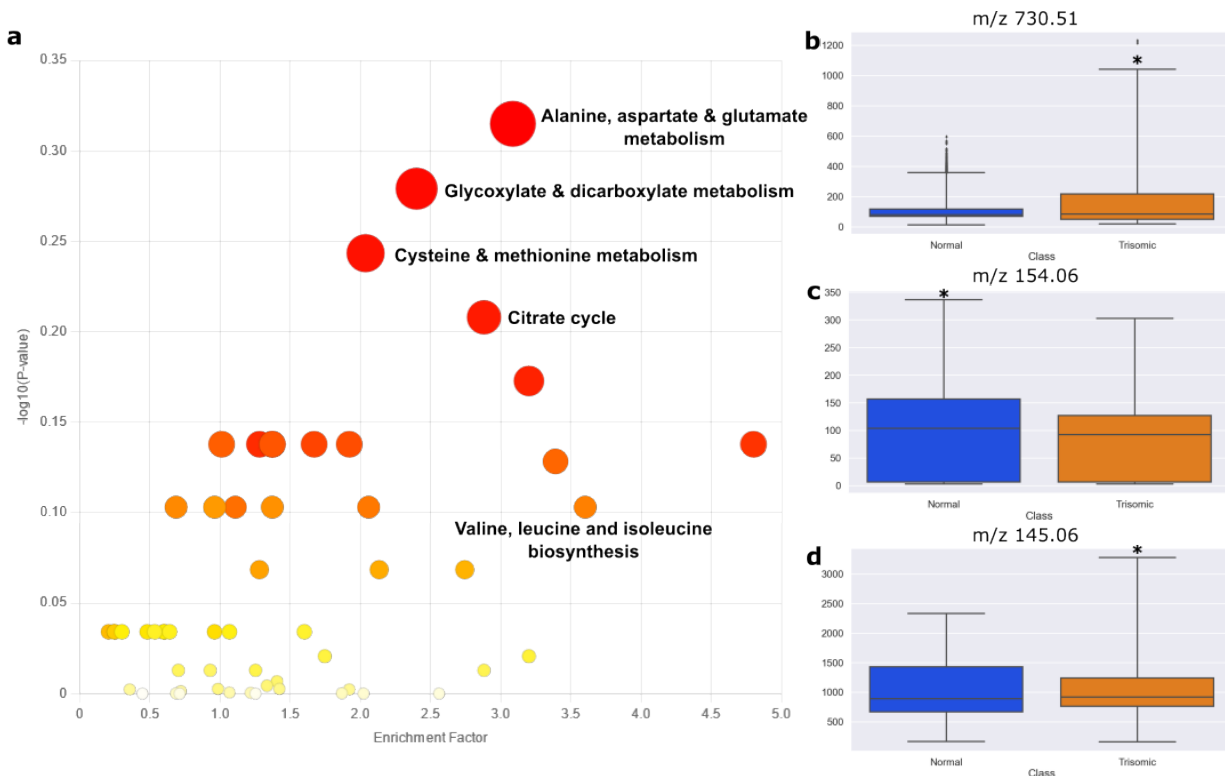


Figure 6: *a)* Metabolic pathway enrichment analysis using the KEGG online database. The logged p -values from the statistical analysis for each metabolic network is indicated on the y -axis, while their corresponding enrichment factor is indicated by the x -axis. *b)-d)* Representative metabolic features that are significantly up-regulated, down-regulated and statistically unchanged respectively between DS and normal mice. m/z 730.51 is tentatively identified as a ceramide which is involved in inflammatory responses in diseases comorbid of DS Worley et al. [2023]; m/z 154.06 is tentatively annotated to be histidine, which has been cited to be reduced significantly in DS human Caracausi et al. [2018], Dierssen et al. [2020]; m/z 145/06 is tentatively identified as glutamine, which has been observed to be unperturbed in terms of bioenergetic pathways of DS Pecze et al. [2020].

scale, it is foreseeable that HyReS may have a major impact on analyses where the resolution of features close to the instrumental limit is vital.

2.5 Assessment of resolution enhancement within physical constraints

To interpret the strong restorative ability of FRCGAN, we further investigate the physical effect of the model on the imaging system, and subsequently evaluate of the possibility of ‘true’ super-resolution, i.e., recovery of novel objects within the image, using only our DL-SISR algorithm. Compared to standard microscopy, some HSI modalities are limited in spatial resolution by physical phenomena that give rise to their contrast mechanism, such as the phonon interaction length Passeri et al. [2023]. In MSI, this is largely instrument-dependent and may even be user-dependent, with traditional methods e.g., MALDI affected by the quality of the matrix. To this end, significant effort has gone towards the development of ambient MSI modalities which require minimal or no sample preparation, making them favourable for direct analysis from soft, biomedical samples. The current technology is however cited to be still lacking in spatial resolution Xiao et al. [2020], thus struggles to provide cellular (μm) level detail that is often essential for life scientists and clinicians.

While we have previously concluded that SOTA SISR models, such as ESRGAN are unlikely to produce any enhancement beyond the instrumental limits Xiang et al. [2023], we revisit the same challenge with the well-trained FRCGAN. We apply FRCGAN to clinical, formalin-fixed paraffin-embedded (FFPE) samples in the form of tissue microarrays (TMA), which has been collected as a part of the larger cohort TransSCOT – a study on thousands of colorectal cancer patients with comprehensive clinicopathological metadata Iveson et al. [2018]. These FFPE TMAs are especially interesting here as the multi-modal spatial analysis of individual cores is expected to expose patient-level heterogeneity of the disease by bridging gaps between multiple sources of complementary information, including

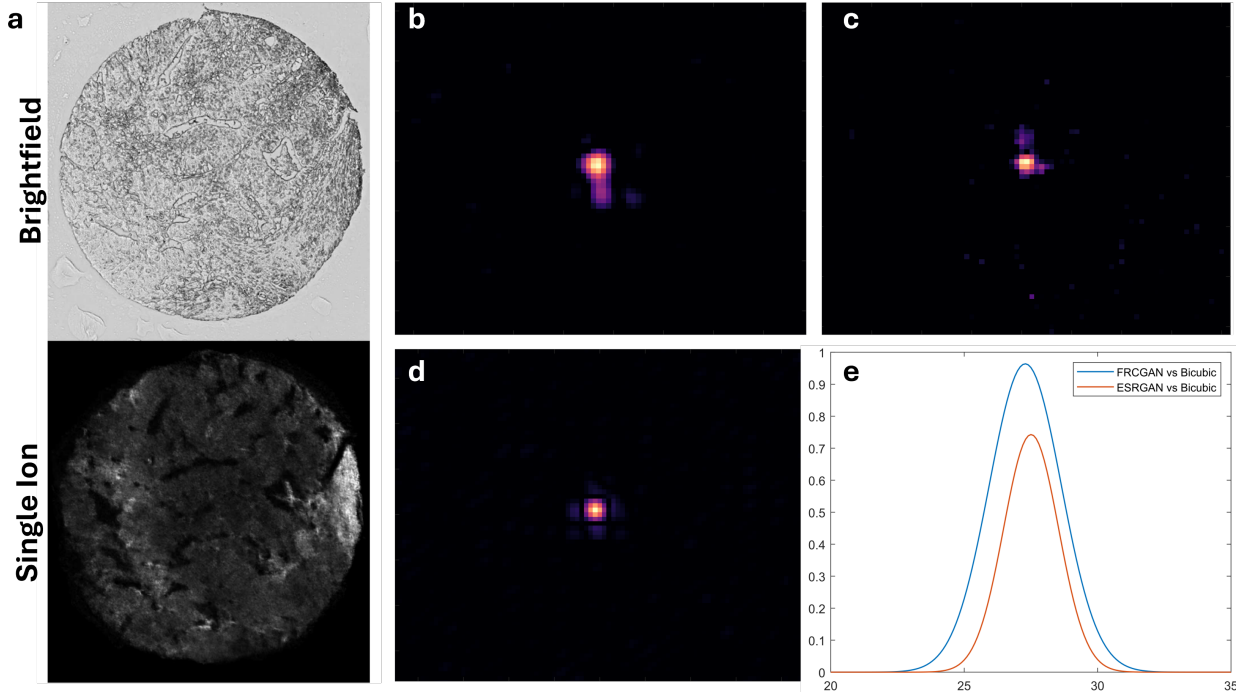


Figure 7: Evaluation of the physical effect of applying HyReS. a) Comparison of super-resolved FPPE core image (m/z 128.0) with the corresponding brightfield optical image. b) the difference PSF obtained from the HyReS-enhanced image shown in a) the same image that was bicubically interpolated. c) the difference PSF obtained from the the same image upsampled by ESRGAN and its bicubically interpolated counterpart. d) The difference PSF between images that were upsampled by our FRCGAN vs the state-of-the-art ESRGAN. e) 2D fits of the Gaussian difference PSFs shown in b) & c), a larger FWHM is clearly visible for FRCGAN, which means a stronger deblurring effect.

genomics, transcriptomics and metabonomics. While ambient MSI can be used to excavate metabolic information, it has traditionally been considered incompatible with FFPE-preserved samples due to a degradation in the signal intensity. This coupled with the order of magnitude mismatch in spatial resolution with corresponding data from techniques such as imaging mass cytometry (IMC) & immunohistochemistry (IHC) are an ideal application for the HyReS approach.

Using a high-resolution imaging setup we have developed in-house using a picosecond laser Battle et al. [2023], a single TMA core has been imaged by LD-REIMS Simon et al. [2023] with a pixel size of $10\mu\text{m}$ and subsequently upsampled by FRCGAN four times on both axes (Figure 7). The network was trained and optimised using our standard approach (Section 4.3). By inspection of Figure 7a, it can be seen that the reconstructed ion image closely resembles the morphology of its corresponding optical image. Owing to the $4\times$ upsampling, a theoretical pixel resolution of $2.5\mu\text{m}$ brings the MSI image to be much more on par with the optical equivalent, which has a pixel resolution of $\sim 1\mu\text{m}$. Using the FRC measure to independently evaluate the effective resolution before and after HyReS, values of $32.92\mu\text{m}$ and $7.71\mu\text{m}$ were yielded respectively, meaning an approximately four-fold enhancement was indeed observed. Due to the nature of our FRC calculation strategy, however, some uncertainty especially when comparing single images are expected, due to for example, under-sampling (Methods).

To remove any method-dependent bias and to visualise the inner-working of the Fourier imaging model underlying FRCGAN, we compute the difference PSF from the results (Methods). First we compare the difference PSF between the FRCGAN-restored image and the original image before upsampling, with the latter resized to the same dimension by simple bicubic interpolation. Interpolation of this kind is known to induce additional blur Liu et al. [2013] and unlikely to provide any gain in resolving power, as such a largely Gaussian difference PSF is obtained (Figure 7b), agreeing with the Fourier model prediction. Similarly, to benchmark our method against the closely related SOTA – ESRGAN, we perform the same calculation between resultant images generated by the two models (Figure 7c). A discernibly Gaussian distribution is still observed in the resultant PSF but with narrower width, indicating much more comparable PSFs in the reconstructed images. While an algebraic ambiguity exist in the sign of the difference calculation, i.e., which PSF is wider, we elucidate this by computing the difference PSF between the ESRGAN-restored image and the interpolated ‘ground truth’. Figure 7c shows the resulting distribution, which is noticeably tighter than

that seen in Figure 7b, indicating inferior deblurring performance. To quantify this, 2D Gaussian fits were carried out on the PSFs compared assuming a rotationally symmetric shape for simplicity (Figure 7e). As a result, it can be shown that FRCGAN outperforms base ESRGAN by a factor of 1.31 in terms of fitted PSF width. In addition, the recovery of the predicted Gaussian functions serves as direct evidence that FRCGAN and to some extent ESRGAN models are performing deconvolution procedures that are routinely used in commercial microscopy to super-resolve images Borlinghaus and Kappel [2016]. Rather than purely enlarging the images, the models have also acquired the ability to remove the effect of a blurry PSF according to the training data, which reiterates the importance of machine learning physically meaningful (PSF-relevant) trends in applying the HyReS approach.

On top of spatial resolution, the main attraction of using HSI for biomedical applications remains the additional spectral contrast. To gain insight into the resolution enhancement enabled by HyReS relative to other concurrent understanding in the field, we compare our results with adjacent IMC data. IMC was performed with a panel of 35 metallic labels on the same patient core from an independent section, a square ROI of $500\ \mu\text{m}^2$ was sampled with a $1\ \mu\text{m}$ pixel size. The results were segmented using an unsupervised approach Li et al. [2015] into 3 main endmembers for visualisation and qualitative comparison with the HyReS-restored AMSI data. By computationally matching a $500\ \mu\text{m}^2$ window ([\[Supplementary Materials\]](#)), visual inspection and direct overlap can be made between the two modalities (Figure 8). In particular, we highlight strong overlap of certain channels from AMSI with the red channel in the segmented IMC image. Despite obvious misalignment in orientation & minor differences in structural details between slides, a reasonable SSIM of ~ 0.37 can be computed between modalities. For example, the ion – m/z 290.0 manifests distinct spatial similarities with the IMC data. Closer assessment of the relative abundance of the channel of interest showed that it mostly correlated with 3 main labels, namely ArAr80, Ir193, Nd143. While the argon is mostly a background channel, the latter two are biological markers. Ir193 is a common DNA intercalator and a specific single-cell marker that rules out debris and doublets Iyer et al. [2022]. Nd143, also known as Vimentin, has been reported as cancer-specific markers and potential therapeutic target Satelli and Li [2011], which would be of direct interest and in line with the motivation of the TransSCOT study. In combination, they demonstrate to our knowledge the first example of such spatial correlation at a cellular level and thus the route to single-cell omics in a biological context, enabled by HyReS. We thus foresee HyReS to be a cornerstone for spatial multi-omics technology of the future, applicable to numerous systems biology approaches that have been revolutionising our understanding.

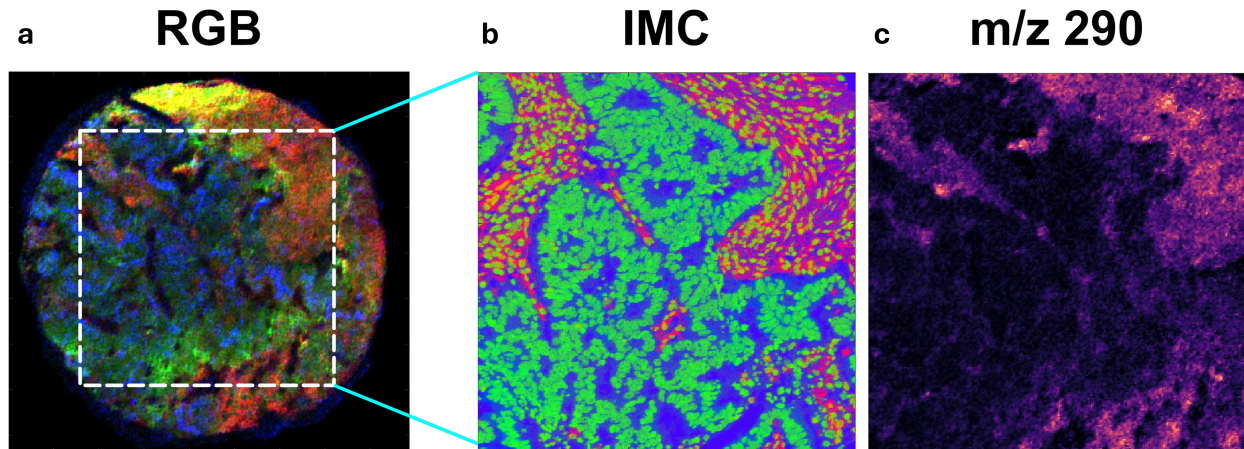


Figure 8: Application of HyReS to single-cell level spatial omics. a) RGB overlay (Red: Green: Blue:) of ion images that have been pixel super-resolved with HyReS. b) Corresponding IMC data obtained from the region indicated with subcellular resolution. c) HyReS-restored data of the ion (m/z 290) which shows high spatial correlation with the red channel in IMC.

3 Discussion

We have demonstrated that HyReS networks trained using the FRCGAN framework can be directly applied to a range of biomedical applications without any prior information nor need of extensive training data. The training strategy makes use of widely applicable inter-data correlations within hyperspectral datasets, which can be readily used to train high-performance models by introducing the understanding of the imaging and noise model without the need of large quantity and variety in training data generation. We show that HyReS can be implemented to address the limitations imposed by the 3S conditions that still restrict HSI in general. Images of whole breast tissue sections can be restored from its synthetically 4-times downsampled input with no obvious degradation to image resolution or quality, the

information richness that usually motivates the use of HSI can also be further verified by segmentation analysis in this case into distinct pathological regions.

We thus foresee the use of HyReS in combination of concurrent mass spectrometry imaging systems to have a major impact for high-throughput applications, such as histopathology. By pre-training networks using images from a higher pixel resolution, HyReS is able to predict and upsample new unseen images taken with larger sampling pixels. This brings about an increase in imaging speed of at least 16 times ($\times 4$ on both axes), allowing point scanning HSI modalities such as DESI to produce whole tissue images in minutes rather than hours without compromising spatial resolution. Even higher upsampling ratios can of course be explored with HyReS, but given the ill-posed nature of this restoration problem Tipping and Bishop [2003], more and deeper understanding of the imaging model will likely be required as prior information, both in terms of training data generation and the imaging formation process that needs to be machine learned.

As well as spatial resolution restoration, we have shown HyReS to have a positive impact in general on downstream image analysis without significantly altering the information content. Apart from the visually apparent denoising effect that has been proven to be generalisable to datasets of diverse origins Xiang et al. [2023], the single image super-resolution process also grants increased data points (pixels) for machine learning tasks while restoring features that are otherwise corrupted by under-sampling, noise and artifact. This has been highlighted by the example of enhanced rate of detection in the genotypic difference in normal and trisomic mouse brains, where the HyReS-enhanced regression model outperforms the original using classification features that are still interpretable. Further validation of these features are of course necessary to draw conclusions on the underlying biology, as the model is reliant on qualitative phenotypic information observed in the detected metabolites. To separate the effect of HyReS and the complex biological processes of interest in such problems, we have also demonstrated the strong generalisability and robustness of trained HyReS models by directly applying them on unseen data from a study of known conclusions. The preservation of the metabolic profiles in the restored mouse brains and the general observation of a strong contrast in the late-stage multiple sclerosis model due to a few identified molecules speak volume to the wide utility of HyReS in future studies of this kind. While we do not recommend using the same HyReS model for all tasks, online training using a portion of new data may be an interesting solution for the future to accumulate restoration power and minimise hallucination, especially when the data changes drastically e.g. new tissue types.

Finally, echoing some existing work Xiang et al. [2023], Qiao et al. [2021], whether HyReS is able to restore novel features i.e. achieving true super-resolution is less certain. To this end, we have investigated the relative effect on the image PSF induced by a HyReS model in accordance with our Fourier imaging model. It is clear that an embedded deconvolution effect is taking place and the quantifiable deblurring achieved in turn amplifies the high spatial frequency content that is already in the image. Akin to confocal microscopy, this may provide more resolving power even though the hardware remains unchanged provided that some signal collection selectivity is in place. In terms of MSI, we have so far omitted the collection path in our proposed imaging model and no such confocal-like models have been formulated to our knowledge, which motivates future work. By measuring PSF information experimentally, sufficient prior information may be obtained to transform HyReS into a true super-resolution HSI tool to go beyond the hardware limitations. Going forward, we envision the combination of HyReS with the development of its corresponding imaging hardware to provide the platform for multimodal studies across scales in the same vein as the FFPE core example given here. Similarly, HyReS can be easily applied to other modes of HSI, e.g. Brillouin microscopy Kabakova et al. [2024] with minimal modification and hence unveils new possibilities that simultaneously demand imaging throughput & resolution.

4 Methods

In this study we aim to learn the mapping from the LR images to their respective HR counterparts while achieving two main restorative effect: denoising and pixel super-resolution. In this section, we briefly introduce three essential components of our study: (1) the imaging experimental methods, (2) the SISR models and (3) the evaluation methods for images and trained models.

4.1 Ambient Mass Spectrometry Imaging

4.1.1 Laser-Desorption Rapid Evaporation Ionisation Mass Spectrometry (LD-REIMS) imaging

Human breast biopsies for synthetic image restoration For LD-REIMS imaging, all experiments utilised a commercially available Opolette HE2731 Optical Parametric Oscillator (Opotek, Carlsbad, USA) running at 20 Hz and tuned to 2.94 μm for mass spectrometry imaging. A distal optical system, assembled from optomechanical components (Thorlabs Inc.) and a CaF₂ lens (LA5315-E) focused the beam onto the sample plane with a diameter of $\sim 60\mu\text{m}$.

Imaging experiments were conducted using a modified two-dimensional stage setup (Prosolia), connected to a Xevo G2-XS QTOF mass spectrometer (Waters Corporation, Milford, MA, USA) controlled by MassLynx 4.1 software (Waters Corporation, Milford, MA, USA). The mass spectrometer featured a prototype REIMS source Jones et al. [2019]. All mass spectrometric analysis was conducted in the negative ion mode within a spectral range of 50-1200 m/z. To demonstrate the concept of image restoration by HyReS, human breast biopsies were imaged using this setup with a pixel size of $100\mu\text{m} \times 100\mu\text{m}$. The resultant images were then downsampled synthetically before restoration during preprocessing (Section 4.3).

Adjacent mouse brain sections for experimental image restoration To experimentally validate HyReS, mouse brain sections were imaged using the same in-house setup. An aspheric lens (C028TME-E, Thorlabs Inc.) was utilised instead of the CaF2 singlet to correct for aberrations. The new beam diameter was measured to be approximately $30\mu\text{m}$ at the sample plane. To create the LR and HR pair, adjacent brain slices that were morphologically similar were independently imaged with pixel sizes of $100\mu\text{m} \times 100\mu\text{m}$ and $25\mu\text{m} \times 25\mu\text{m}$ respectively.

High-resolution LD-REIMS imaging of FFPE TMA core. For high-resolution, a prototype optical parametric amplifier (OPA) system operating in the picosecond regime Battle et al. [2023] was used in place of the OPO from previous LD-REIMS experiments while all other components were identical. Briefly, the OPA system consists of a high power pump laser and a nonlinear crystal to achieve amplification through parametric interaction. A pulsed microchip laser operating at $1.06\mu\text{m}$ with a repetition rate of 500 kHz is amplified by an ytterbium (Yb)-doped fiber amplifier (YDFA). The output from the YDFA is used as the pump laser, providing a pulse energy of $6\mu\text{J}$ for the amplification process. A seed signal at a wavelength of $1.67\mu\text{m}$ is introduced into the nonlinear crystal, which is magnesium (Mg)-doped Periodically Poled Lithium Niobate (PPLN) crystal. The crystal is designed with a poling period of $31\mu\text{m}$ to phase match the pump and seed wavelengths, enabling efficient energy transfer from the pump to the seed and generating an amplified output signal and an idler at the wavelength of $2.94\mu\text{m}$. The pump and the seed beams are focused into the PPLN crystal using an N-BK7 lens with $f = 125\text{mm}$. The PPLN crystal is mounted on a temperature-controlled oven and held at a fixed temperature of 164°C to maintain optimal phase matching conditions. The output beams are then collimated by a calcium fluoride (CaF2) lens with $f = 200\text{mm}$ for further use in the REIMS imaging. The idler is centered at $2.94\mu\text{m}$ with a pulse duration of 100 ps, and a pulse energy of 400 nJ is delivered to the samples.

A single TMA core from an anonymised patient with corresponding IMC data was imaged with a pixel size of $10\mu\text{m} \times 10\mu\text{m}$ before upsampling by HyReS.

4.1.2 Desorption Electro-Flow Focusing Ionization (DEFFI) imaging

Brain sections from Down Syndrome mouse model. Ts65Dn mice (JAX stock no. 001924, B6EiC3Sn *a/A - Ts(1716)65Dn/J*) mice were purchased from Charles River, the mouse colony was amplified and maintained at the Animal Facilities of the Barcelona Biomedical Research Park (PRBB, Barcelona, Spain, EU). All animal procedures met the guidelines of the European Community Directive 86/609/EEC and were approved by the Local Ethics Committee. Following breedings, the offspring were genotyped along the weaning stage, and segregated or co-housed, in sex-separated groups of 4-5 mice. Adult mice (4 months-old) were euthanized in a CO2 euthanasia chamber, immediately followed by brain hemispheres dissection, snap-freezing in liquid N2, and sample storage at -80°C . All samples were cryosectioned at $10\mu\text{m}$ thickness using a Microm HM 550 Cryostat (Thermo Fisher Scientific Inc., Waltham, USA). Tissue sections were thaw-mounted onto SuperFrost Plus Glass slides (Thermo Fisher Scientific Inc., Waltham, USA). Tissue sections were stored at -80°C until further use. An enhanced desorption electrospray ionisation (DESI) imaging setup previously reported Wu et al. [2022] was used for imaging of brain samples, using a commercially available DESI source (Waters Corporation) and previously optimised parameters Tillner et al. [2017]. The sprayer utilised a TaperTip capillary measuring $20\mu\text{m}$ internally and $363\mu\text{m}$ externally, operating at a 75° angle relative to the surface plane. It maintained distances of 5 mm from the sprayer to the inlet capillary and 1 mm from the sprayer to the surface, while applying a high voltage of 4.5 kV. A solvent mixture of methanol/water, 95:5 (v/v), was supplied by a nanoAcquity binary solvent manager (Waters, Wilmslow, UK) at a flow rate of $1.5\mu\text{L}/\text{min}$ and an inlet gas pressure of 5 bar (nitrogen). As the DEFFI sprayer was based on the same commercially available Waters DESI sprayer, the geometric configuration remained consistent. The final parameters for tissue imaging with DEFFI were established as follows: employing a TaperTip capillary with inner and outer diameters of $20\mu\text{m}$ and $363\mu\text{m}$ respectively, maintaining a capillary-to-orifice distance of $100\mu\text{m}$, and utilizing an exit orifice diameter of $150\mu\text{m}$. The solvent flow rate was adjusted to $0.75\mu\text{L}/\text{min}$ – $1.5\mu\text{L}/\text{min}$ of methanol/water, 95:5 (v/v), with an inlet gas pressure of 5 bar (nitrogen) and a high voltage of 4.5 kV. All mass spectrometric analysis was conducted in the negative ion mode within a spectral range of 50-1200 m/z. All Down Syndrome mouse brain sections were imaged with a pixel size of $75\mu\text{m} \times 75\mu\text{m}$ before upsampling by HyReS.

Spinal cord sections from EAE mouse model. Spinal cord sections of both control and acute EAE mice were imaged using the DEFFI system with a pixel size of $70\ \mu\text{m} \times 70\ \mu\text{m}$ for the study reported in Peruzzotti-Jametti et al. [2024]. The same dataset was downsampled during preprocessing and then restored by HyReS to evaluate its effect on the biological information extracted.

4.2 Optical Imaging

To generate the reference images for pathological assessment, consecutive slides obtained from the same sample sets (human breast, EAE mouse and FFPE TMA) used for MSI were H&E-stained and scanned with a digital slide scanner (NanoZoomer2.0-HT, Hamamatsu City, Japan). A high-resolution objective ($40\times$) was used for all slides. After an initial autofocus procedure to identify the optimal focal positions of the cores, each slide was imaged within 10–20 min depending on the size of the effective ROI.

4.3 Data Preprocessing

Training data are first filtered to remove extremely low SNR images. The SNR is calculated by the mean squared error (MSE) in Equation 1 between the image and pure black background, where, D represents the matrix of the image and B represents the matrix of the black background, m represents the numbers of rows and i represents the index of that row of the image. n represents the number of columns and j represents the index of that column of the image. The background matrix only consists of zeros and therefore is discarded in the final equation.

$$MSE = \frac{1}{mn} \sum_{i=0}^{m-1} \sum_{j=0}^{n-1} (D(i, j) - B(i, j))^2 = \frac{1}{mn} \sum_{i=0}^{m-1} \sum_{j=0}^{n-1} D(i, j)^2 \quad (1)$$

To enable FRCGAN training with only one set of images, the LR counterparts are manually created from the original input dataset. For the restoration tasks attempted in this study with both synthetic and experimental data, first the images are cropped on both axes to be divisible by the scaling factor, in this case 4. Next the images in the original dataset are downsampled using the standard bicubic kernel to create the LR counterparts that are 16 times smaller. To account for noise in the imaging system, additive noises approximated to be Gaussian ([Supplementary]) are applied to the downsampled LR images. Moreover we select a number of images randomly from the dataset and add noise to both their images and backgrounds as shown in the [Supplementary Materials].

4.4 SISR Network Architecture and Training

HyReS utilises a SOTA GAN-based architecture for SISR (Real-ESRGAN) Wang et al. [2021] that has achieved photo-realistic restoration and upsampling in natural images, which consists of a Generator and a Discriminator model. The Generator restores and upscales each LR input image and the resulting HR output image is then assessed by the Discriminator. The two models function hand-in-hand to iteratively improve the quality of the images generated by optimising some loss function. While common GAN-based SISR algorithms, including the real-ESRGAN assess the image quality based on some pixel-wise metric (e.g., L1 & L2 norm), we have previously observed that they do not reflect the underlying imaging performance Xiang et al. [2023] but rather based on some subjective perception of relative image quality.

To achieve objective improvement in resolution for bioimaging by DL-SISR, we have implemented two main modifications. Firstly, for all image restoration tasks, the Real-ESRGAN is fine-tuned using the MSI data such that the dimensions of the resulted image are the same compared with the HR by simple reshaping. Additionally, to train models that are relevant in the scope of the physical imaging model (Sec. 4.5), we have implemented a novel loss. This new loss (\mathcal{L}_{FRC}) is based on Fourier Ring Correlation (FRC) Koho et al. [2019],

$$\text{FRC}(r) = \frac{\sum_r F_1(r) \cdot F_2(r)^*}{\sqrt{\sum_r F_1^2(r) \cdot \sum_r F_2^2(r)}} \quad (2)$$

where the r_i is the frequency bin and F_i is the Fourier transform of image i . This effectively estimates the resolution of each image in frequency space with the consideration of noise and ensures relative improvement between input and output images, whereby:

$$\mathcal{L}_{\text{FRC}} = 1 - \sum_r \text{FRC}(r) \quad (3)$$

where r is the frequency bin used in Fourier space. The new FRC loss has been checked to be differentiable and is therefore a well-defined loss. We have thus named this strategy FRCGAN. \mathcal{L}_{FRC} is minimised in the Generator of the

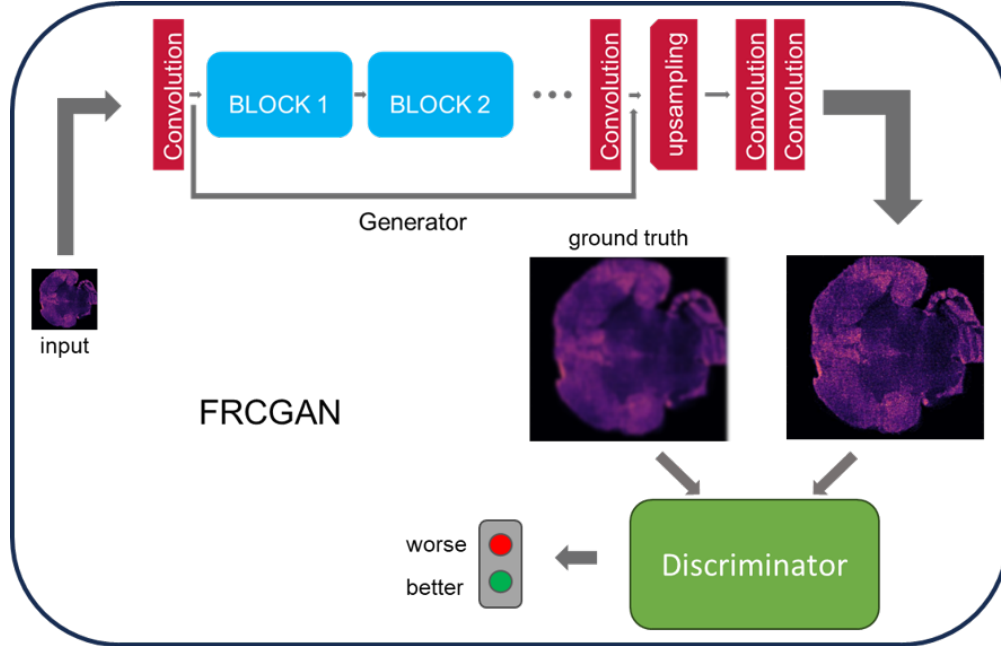


Figure 9: Architecture of FRCGAN and schematic workflow of HyReS.

architecture for all applications reported, while the Discriminator is still optimised via the Cross Entropy loss due to constraints in computational intensity. However, we expect that fast, probabilistic implementation into the Discriminator part of the network is feasible and may yield even better performance.

During training of the FRCGAN models, the Adam optimiser was used which yielded the following hyperparameter combination that produced the best upsampling performance: number of epochs = 100, batch size = 8, generator loss = \mathcal{L}_{FRC} , discriminator loss = Cross Entropy, discriminator initial weight = 0 and patch size = 50.

4.5 Evaluation Methods

We implement a combination of computational metrics, physical property, and biological implications to assess the restored images and the performance of the corresponding deep learning model.

4.5.1 Image Quality Metrics

Referenceless metrics. Although human observers can subjectively examine the restored images, image quality assessment (IQA) metrics are used in this work to quantitatively evaluate the performances of different SR models. The most common IQA metrics are full-reference metrics (comparing the test image against the reference image), for example, peak-signal-to-noise ratio (PSNR) and structural similarity index measure (SSIM). The PSNR calculates the image quality using a transform of the mean square error (MSE), and the SSIM is designed as a measure of structure, luminance, and contrast rather than the traditional error summation Hore and Ziou [2010]. There are also no-reference IQA metrics available (only using the test image for evaluation), for instance, blind/referenceless image spatial quality evaluator (BRISQUE) Mittal et al. [2012] and perception based image quality evaluator (PIQE) Venkatanath et al. [2015], for better estimating the perceptual quality of predicted images. BRISQUE is an opinion-aware metric, and it requires a pre-trained model. The training images have known distortions, like artifacts, blurring and noise, and they have been marked with subjective quality scores. In contrast, PIQE is an opinion-unaware and unsupervised metric, which does not need any pre-training. PIQE can evaluate images with arbitrary distortion.

The two referenceless metrics may disagree if the pretrained data set for BRISQUE diverge from the data set of interest thus results in difficult interpretation. We propose a new IQA metric CRISQUE, constrained referenceless image spatial quality evaluator, as a combination of BRISQUE and PIQE:

$$\text{CRISQUE} = \left(1 - 2 \times \frac{1}{\frac{1}{\text{BRISQUE}} + \frac{1}{\text{PIQE}}} \right) \times 100\% \quad (4)$$

The fraction that takes both BRISQUE and PIQE into account is analogous to the resistance of two parallel resistors. This formulation ensures that CRISQUE is bounded between 0 and 100% and can be easily interpreted as it increases as the image quality improves. Most importantly, when comparing SR with LR/HR with known ground truths, if BRISQUE increases (worse image quality), as long as PIQE decreases (better image quality) by equal or larger amount, the total score by CRISQUE still increases (better image quality).

4.5.2 Image Resolution

The limiting resolution of an imaging system is typically defined instrumentally and fundamentally related to the amount of information obtainable Ober et al. [2004]. Hyperspectral imaging is no different, as we have previously reported a linear imaging model for MSI Metodiev et al. [2021]:

$$\text{Detected Signal} = \text{True Signal} \otimes \text{Reponse} + \text{Noise} \quad (5)$$

where the acquired image can be seen as undergoing a blurring process, defined by a system response function, also known as the point spread function (PSF). The blurred image is then further corrupted by additive noise. While the standardisation of resolution remains an ongoing topic of discussion, we have previously presented a simple metric in the form of Fourier ring correlation Xiang et al. [2023] that can estimate the PSF from a single image. Namely, the FRC between two images is defined as the following: While two images are needed conventionally to compute FRC, here we adopt an approach that sub-divides each image into two sub-sampled images for FRC calculation Koho et al. [2019]. As well as providing a quantifiable measure of image resolution that is physically relevant, this metric is also embedded into our image restoration algorithms as a novel loss function (Section 4.4).

4.5.3 Difference Point Spread Function

To generalise our physical imaging model and benchmark the performance of FRCGAN against the state-of-the-art, we derive a new metric that reflects the relative improvement to the imaging PSF. According to our proposed model (Eq. 5), any raw image (I) of the object (O) in a hyperspectral dataset can be described by:

$$I = O \otimes PSF + N \quad (6)$$

After applying an image restoration operation via FRCGAN or otherwise, we expect a direct impact on the PSF and noise (N) such that:

$$I' = O \otimes PSF' + N' \quad (7)$$

where the restored image I' is now convolved with a new system response (PSF') and noise level (N'). To quantify this change, we first Fourier transform both the original and restored image and then take the ratio, which allows the use of well-known Fourier relations to cancel out the object function such that:

$$\frac{\hat{I}}{\hat{I}'} = \frac{M}{M'} + const \quad (8)$$

where the Fourier transform operation is denoted by $\hat{\cdot}$. This gives rise to the Fourier-domain PSF, which is typically defined as the modulus transfer function (M) of the system and a constant term based on the assumption of white noise.

As we have previously reported a Gaussian PSF model in terms of MSI Metodiev et al. [2021], a new metric that measures the relative change in the imaging performance can be defined by taking the inverse Fourier transform:

$$PSF_d = F^{-1}\left(\frac{\hat{I}}{\hat{I}'}\right) \quad (9)$$

We name this metric the difference point spread function and use it to visualise the effect of HyReS and other restoration processes in a physically meaningful manner.

4.6 Image Analysis

4.6.1 Segmentation

UMAP is a nonlinear dimensionality reduction technique that projects the high-dimensional data to a low-dimensional space while retaining the overall structures of the original data. Here 2D UMAP embeddings of MSI data were generated for spatial clustering with the following hyperparameters, which have been empirically optimised: (initialisation = spectral embedding of fuzzy 1-skeleton McInnes et al. [2018], dimension = 2, number of neighbours = 20, distance metric = cosine, minimum distance between embedded points = 0.2).

The resultant embeddings were then clustered using HDBSCAN, whose hyperparameters were also empirically optimised to best yield a pre-defined number of clusters for all analyses: (minimum sample size = 100, minimum cluster size = 300, cluster selection method = Excess of Mass).

4.6.2 Classification

We also assessed if the restored images retain the biological features of the original images in terms of classification tasks. The regions of interests were selected manually from the original and upsampled bicubically for application in images that underwent pixel super-resolution (Section 2.4). The pixel intensities for different (m/z) channels (aligned to 100 ppm) were then taken to train support vector machine (SVM) models, which were then evaluated by cross-validation (10-fold) and/or testing on independent data. The classification performance was generally evaluated by weighted accuracy Mosley [2013]. The whole spectral range was used for model training in the first iteration, to maximise model interpretability and the robustness of the model, we then performed recursive feature elimination (RFE) to select the only significant classification features which were used to train the optimised models. The hyperparameters in RFE were optimised through a grid search to determine the minimum features to select. For the classification of trisomy (Section 2.4), we applied the optimised trained models first on whole brain tissue images (including regions unseen in training) that they were trained on and then independent brain images. A pixelwise probability was computed by the model as result in each case to generate heatmaps ([Supplementary]), which was then used to label the whole tissue to be either trisomic or normal. This was assigned according to a percentage pixel threshold e.g., 50% of all pixels pertaining to a tissue region in order for it to be classified. The threshold was adaptively optimised for each slide image (4 brains per slide) to yield the highest tissue-wise classification performance. For the whole tissue classification by GT and HyReS-enhanced images, the thresholds were set to be (10%, 10%, 30%, 20%) and (10%, 10%, 30%, 30%) respectively. For the independent test, the thresholds were 10% (GT) and 20% (HyReS).

Acknowledgements

The authors thank C.K.L.Seow and D.Stoddart for the insightful discussions. We thank M.Wang for helping and curating the associated Github repository. Y.X, Z.T would like to thank the financial support from the CRUK Rosetta Grand Challenge (A25045, A24034, A25043, A25038) and BBSRC (BB/X004082/1) during this research. R.T.M was supported by the Engineering and Physical Sciences Research Council (EPSRC) (EP/W029251/1). Z.L also acknowledges support by the EPSRC under grant EP/N014529/1 funding the EPSRC Centre for Mathematics of Precision Healthcare at Imperial College London. L.P.J was supported by funding from the Wellcome Trust Clinical Research Career Development Fellowship (G105713), Evelyn Trust Grant under the project reference 24/08 Med-24-2313, National MS Society Grant (RFA-2203-39318) and Medical Research Council (MRC) Clinician Scientist Fellowship (MR/Z50659X/1). M.E.G.S was supported by a School of Clinical Medicine Cambridge Trust Scholarship and the MRC Doctoral Training Grant (RG86932).

Author contributions

Y.X and Z.L contributed equally to this manuscript and share first authorship. Y.X conceived and initiated the research. Y.X, Z.L, B.C designed, trained and validated the DL-SISR methods. D.S, V.W, K.R, Y.W, R.B acquired experimental data. R.T.M provided access to the high-resolution imaging setup. M.E.G.S and L.P.J acquired data and analyses on MS mouse models. X.A provided the DS mouse models. Y.X and Z.T supervised the project. The manuscript writing was led by Y.X and Z.L with contributions and editing from all authors.

References

- Himar Fabelo, Samuel Ortega, Daniele Ravi, B. Ravi Kiran, Coralía Sosa, Diederik Bulters, Gustavo M. Callicó, Harry Bulstrode, Adam Szolna, Juan F. Piñeiro, Silvester Kabwama, Daniel Madroñal, Raquel Lazcano, Aruma J-O'Shanahan, Sara Bisshopp, María Hernández, Abelardo Báez, Guang-Zhong Yang, Bogdan Stanciulescu, Rubén Salvador, Eduardo Juárez, and Roberto Sarmiento. Spatio-spectral classification of hyperspectral images for brain cancer detection during surgical operations. *PLOS ONE*, 13(3):e0193721, mar 2018. ISSN 1932-6203. doi:10.1371/journal.pone.0193721. URL <https://dx.plos.org/10.1371/journal.pone.0193721>.
- Jonghee Yoon. Hyperspectral Imaging for Clinical Applications. *BioChip Journal*, 16(1):1–12, mar 2022. ISSN 1976-0280. doi:10.1007/s13206-021-00041-0. URL <https://link.springer.com/10.1007/s13206-021-00041-0>.
- Prachi Singh, Prem Chandra Pandey, George P. Petropoulos, Andrew Pavlides, Prashant K. Srivastava, Nikos Koutsias, Khidir Abdala Kwal Deng, and Yangson Bao. Hyperspectral remote sensing in precision agriculture: present status, challenges, and future trends. In *Hyperspectral Remote Sensing*, pages 121–146. Elsevier, 2020. doi:10.1016/B978-0-08-102894-0.00009-7. URL <https://linkinghub.elsevier.com/retrieve/pii/B9780081028940000097>.
- Irina Kabakova, Jitao Zhang, Yuchen Xiang, Silvia Caponi, Alberto Bilenca, Jochen Guck, and Giuliano Scarcelli. Brillouin microscopy. *Nature Reviews Methods Primers*, 4(1):8, feb 2024. ISSN 2662-8449. doi:10.1038/s43586-023-00286-z. URL <https://www.nature.com/articles/s43586-023-00286-z>.
- Robin R. Jones, David C. Hooper, Liwu Zhang, Daniel Wolverson, and Ventsislav K. Valev. Raman Techniques: Fundamentals and Frontiers. *Nanoscale Research Letters*, 14(1):231, dec 2019. ISSN 1931-7573. doi:10.1186/s11671-019-3039-2. URL <https://nanoscalereslett.springeropen.com/articles/10.1186/s11671-019-3039-2>.
- Justin M. Wiseman, Demian R. Ifa, Qingyu Song, and R. Graham Cooks. Tissue Imaging at Atmospheric Pressure Using Desorption Electrospray Ionization (DESI) Mass Spectrometry. *Angewandte Chemie International Edition*, 45(43):7188–7192, nov 2006. ISSN 14337851. doi:10.1002/anie.200602449. URL <https://onlinelibrary.wiley.com/doi/10.1002/anie.200602449>.
- Daniel Simon, Gabriel Stefan Horkovics-Kovats, Yuchen Xiang, Julia Abda, Dimitris Papanastasiou, Hui-Yu Ho, Haixing Wang, Richard Schäffer, Anna Mroz, Laurine Lagache, Julia Balog, Isabelle Fournier, Josephine Bunch, and Zoltan Takats. Sample preparation free tissue imaging using Laser Desorption – Rapid Evaporative Ionisation Mass spectrometry (LD-REIMS). *ChemRxiv*, 2023. doi:10.26434/chemrxiv-2023-p2g9h-v2.
- Yipo Xiao, Jiewei Deng, Yao Yao, Ling Fang, Yunyun Yang, and Tiangang Luan. Recent advances of ambient mass spectrometry imaging for biological tissues: A review. *Analytica Chimica Acta*, 1117:74–88, 2020. ISSN 18734324. doi:10.1016/j.aca.2020.01.052. URL <https://doi.org/10.1016/j.aca.2020.01.052>.
- Mohammad Abdo, Vlad Badilita, and Jan Korvink. Spatial scanning hyperspectral imaging combining a rotating slit with a Dove prism. *Optics Express*, 27(15):20290, 2019. ISSN 1094-4087. doi:10.1364/oe.27.020290.
- Jinjuan Xue, Yu Bai, and Huwei Liu. Recent advances in ambient mass spectrometry imaging. *TrAC - Trends in Analytical Chemistry*, 120:115659, 2019. ISSN 18793142. doi:10.1016/j.trac.2019.115659. URL <https://doi.org/10.1016/j.trac.2019.115659>.
- Vincen Wu, Jocelyn Tillner, Emrys Jones, James S. McKenzie, Dipa Gurung, Anna Mroz, Liam Poynter, Daniel Simon, Cristina Grau, Xavier Altafaj, Marc-Emmanuel Dumas, Ian Gilmore, Josephine Bunch, and Zoltan Takats. High Resolution Ambient MS Imaging of Biological Samples by Desorption Electro-Flow Focussing Ionization. *Analytical Chemistry*, 94(28):10035–10044, jul 2022. ISSN 0003-2700. doi:10.1021/acs.analchem.2c00345. URL <https://pubs.acs.org/doi/10.1021/acs.analchem.2c00345>.
- Raf Van de Plas, Junhai Yang, Jeffrey Spraggins, and Richard M. Caprioli. Image fusion of mass spectrometry and microscopy: a multimodality paradigm for molecular tissue mapping. *Nature Methods*, 12(4):366–372, apr 2015. ISSN 1548-7091. doi:10.1038/nmeth.3296. URL <http://www.nature.com/articles/nmeth.3296>.
- Hang Hu and Julia Laskin. Emerging Computational Methods in Mass Spectrometry Imaging. *Advanced Science*, 9(34):1–20, 2022. ISSN 21983844. doi:10.1002/advs.202203339.
- Gao Huang, Zhuang Liu, Geoff Pleiss, Laurens van der Maaten, and Kilian Q. Weinberger. Convolutional Networks with Dense Connectivity. *IEEE Transactions on Pattern Analysis and Machine Intelligence*, 44(12):8704–8716, dec 2022. ISSN 0162-8828. doi:10.1109/TPAMI.2019.2918284. URL <https://ieeexplore.ieee.org/document/8721151/>.
- Christian Ledig, Lucas Theis, Ferenc Huszar, Jose Caballero, Andrew Cunningham, Alejandro Acosta, Andrew Aitken, Alykhan Tejani, Johannes Totz, Zehan Wang, and Wenzhe Shi. Photo-Realistic Single Image Super-Resolution Using a Generative Adversarial Network. sep 2016. URL <http://arxiv.org/abs/1609.04802>.

- Xintao Wang, Ke Yu, Shixiang Wu, Jinjin Gu, Yihao Liu, Chao Dong, Yu Qiao, and Chen Change Loy. ESRGAN: Enhanced super-resolution generative adversarial networks. *Lecture Notes in Computer Science (including subseries Lecture Notes in Artificial Intelligence and Lecture Notes in Bioinformatics)*, 11133 LNCS:63–79, 2019. ISSN 16113349. doi:10.1007/978-3-030-11021-5_5.
- Xintao Wang, Liangbin Xie, Chao Dong, and Ying Shan. Real-ESRGAN: Training Real-World Blind Super-Resolution with Pure Synthetic Data. jul 2021. URL <http://arxiv.org/abs/2107.10833>.
- Martin Weigert, Uwe Schmidt, Tobias Boothe, Andreas Müller, Alexandr Dibrov, Akanksha Jain, Benjamin Wilhelm, Deborah Schmidt, Coleman Broaddus, Siân Culley, Mauricio Rocha-Martins, Fabián Segovia-Miranda, Caren Norden, Ricardo Henriques, Marino Zerial, Michele Solimena, Jochen Rink, Pavel Tomancak, Loic Royer, Florian Jug, and Eugene W. Myers. Content-aware image restoration: pushing the limits of fluorescence microscopy. *Nature Methods*, 15(12):1090–1097, 2018. ISSN 15487105. doi:10.1038/s41592-018-0216-7. URL <http://dx.doi.org/10.1038/s41592-018-0216-7>.
- Chang Qiao, Di Li, Yuting Guo, Chong Liu, Tao Jiang, Qionghai Dai, and Dong Li. Evaluation and development of deep neural networks for image super-resolution in optical microscopy. *Nature Methods*, 18(2):194–202, feb 2021. ISSN 1548-7091. doi:10.1038/s41592-020-01048-5. URL <http://www.nature.com/articles/s41592-020-01048-5>.
- Yuchen Xiang, Martin Metodiev, Meiqi Wang, Boxuan Cao, Josephine Bunch, and Zoltan Takats. Enhancement of Ambient Mass Spectrometry Imaging Data by Image Restoration. *Metabolites*, 13(5):669, may 2023. ISSN 2218-1989. doi:10.3390/metabo13050669. URL <https://www.mdpi.com/2218-1989/13/5/669>.
- Tiepeng Liao, Zihao Ren, Zhaoliang Chai, Man Yuan, Chenjian Miao, Junjie Li, Qi Chen, Zhilin Li, Ziyi Wang, Lin Yi, Siyuan Ge, Wenwei Qian, Longfeng Shen, Zilei Wang, Wei Xiong, and Hongying Zhu. A super-resolution strategy for mass spectrometry imaging via transfer learning. *Nature Machine Intelligence*, 5(6):656–668, 2023. ISSN 25225839. doi:10.1038/s42256-023-00677-7.
- Leland McInnes, John Healy, and James Melville. UMAP: Uniform Manifold Approximation and Projection for Dimension Reduction. 2018. URL <http://arxiv.org/abs/1802.03426>.
- Martin Ester, Hans-Peter Kriegel, Jörg Sander, and Xiaowei Xu. A Density-Based Algorithm for Discovering Clusters a Density-Based Algorithm for Discovering Clusters in Large Spatial Databases with Noise. In *Proceedings of the Second International Conference on Knowledge Discovery and Data Mining, KDD’96*, pages 226–231. AAAI Press, 1996.
- Martin D. Metodiev, Rory T. Steven, Xavier Loizeau, Zoltan Takats, and Josephine Bunch. Modality Agnostic Model for Spatial Resolution in Mass Spectrometry Imaging: Application to MALDI MSI Data. *Analytical Chemistry*, 93(46):15295–15305, nov 2021. ISSN 0003-2700. doi:10.1021/acs.analchem.1c02470. URL <https://pubs.acs.org/doi/10.1021/acs.analchem.1c02470>.
- Luca Peruzzotti-Jametti, Cory M. Willis, Regan Hamel, Grzegorz Krzak, and Stefano Pluchino. Metabolic Control of Smoldering Neuroinflammation. *Frontiers in Immunology*, 12(June):1–16, 2021. ISSN 16643224. doi:10.3389/fimmu.2021.705920.
- L. Peruzzotti-Jametti, C. M. Willis, G. Krzak, R. Hamel, L. Pirvan, R.-B. Ionescu, J. A. Reisz, H. A. Prag, M. E. Garcia-Segura, V. Wu, Y. Xiang, B. Barlas, A. M. Casey, A. M. R. van den Bosch, A. M. Nicaise, L. Roth, G. R. Bates, H. Huang, P. Prasad, A. E. Vincent, C. Frezza, C. Viscomi, G. Balmus, Z. Takats, J. C. Marionni, A. D’Alessandro, M. P. Murphy, I. Mohorianu, and S. Pluchino. Mitochondrial complex I activity in microglia sustains neuroinflammation. *Nature*, 628(8006):195–203, apr 2024. ISSN 0028-0836. doi:10.1038/s41586-024-07167-9. URL <https://www.nature.com/articles/s41586-024-07167-9>.
- Mohammed Rachidi and Carmela Lopes. Mental retardation in Down syndrome: From gene dosage imbalance to molecular and cellular mechanisms. *Neuroscience Research*, 59(4):349–369, dec 2007. ISSN 01680102. doi:10.1016/j.neures.2007.08.007. URL <https://linkinghub.elsevier.com/retrieve/pii/S0168010207017464>.
- Mara Dierssen, Marta Fructuoso, María Martínez de Lagrán, Marzia Perluigi, and Eugenio Barone. Down Syndrome Is a Metabolic Disease: Altered Insulin Signaling Mediates Peripheral and Brain Dysfunctions, jul 2020. ISSN 1662453X.
- Noemí Rueda, Jesús Flórez, and Carmen Martínez-Cué. Mouse Models of Down Syndrome as a Tool to Unravel the Causes of Mental Disabilities. *Neural Plasticity*, 2012:1–26, 2012. ISSN 2090-5904. doi:10.1155/2012/584071. URL <http://www.hindawi.com/journals/np/2012/584071/>.
- Jarid Goodman and Mark G. Packard. The role of the dorsal striatum in extinction: A memory systems perspective. *Neurobiology of Learning and Memory*, 150:48–55, apr 2018. ISSN 10747427. doi:10.1016/j.nlm.2018.02.028.

- Shuzhao Li, Youngja Park, Sai Duraisingham, Frederick H. Strobel, Nooruddin Khan, Quinlyn A. Soltow, Dean P. Jones, and Bali Pulendran. Predicting Network Activity from High Throughput Metabolomics. *PLoS Computational Biology*, 9(7):e1003123, jul 2013. ISSN 1553-7358. doi:10.1371/journal.pcbi.1003123. URL <https://dx.plos.org/10.1371/journal.pcbi.1003123>.
- Shaoli Cai, Jinxin Lin, Zhaolong Li, Songnian Liu, Zhihua Feng, Yangfan Zhang, Yanding Zhang, Jianzhong Huang, and Qi Chen. Alterations in intestinal microbiota and metabolites in individuals with Down syndrome and their correlation with inflammation and behavior disorders in mice. *Frontiers in Microbiology*, 14, feb 2023. ISSN 1664-302X. doi:10.3389/fmicb.2023.1016872.
- Maria Caracausi, Veronica Ghini, Chiara Locatelli, Martina Mericio, Allison Piovesan, Francesca Antonaros, Maria Chiara Pelleri, Lorenza Vitale, Rosa Anna Vacca, Federica Bedetti, Maria Chiara Mimmi, Claudio Luchinat, Paola Turano, Pierluigi Strippoli, and Guido Cocchi. Plasma and urinary metabolomic profiles of Down syndrome correlate with alteration of mitochondrial metabolism. *Scientific Reports*, 8(1):2977, feb 2018. ISSN 2045-2322. doi:10.1038/s41598-018-20834-y.
- Gordon Worley, Seul Kee Byeon, P. Brian Smith, Sarah J. Hart, Sarah P. Young, Akhilesh Pandey, and Priya S. Kishnani. An exploratory study of plasma ceramides in comorbidities in Down syndrome. *American Journal of Medical Genetics Part A*, 191(9):2300–2311, sep 2023. ISSN 1552-4825. doi:10.1002/ajmg.a.63325.
- Laszlo Pecze, Elisa B. Randi, and Csaba Szabo. Meta-analysis of metabolites involved in bioenergetic pathways reveals a pseudohypoxic state in Down syndrome. *Molecular Medicine*, 26(1):102, dec 2020. ISSN 1076-1551. doi:10.1186/s10020-020-00225-8.
- A.A. Passeri, A. Di Michele, I. Neri, F. Cottone, D. Fioretto, M. Mattarelli, and S. Caponi. Size and environment: The effect of phonon localization on micro-Brillouin imaging. *Biomaterials Advances*, 147:213341, apr 2023. ISSN 27729508. doi:10.1016/j.bioadv.2023.213341. URL <https://linkinghub.elsevier.com/retrieve/pii/S277295082300064X>.
- Timothy J Iveson, Rachel S Kerr, Mark P Saunders, Jim Cassidy, Niels Henrik Hollander, Josep Taberner, Andrew Haydon, Bengt Glimelius, Andrea Harkin, Karen Allan, John McQueen, Claire Scudder, Kathleen Anne Boyd, Andrew Briggs, Ashita Waterston, Louise Medley, Charles Wilson, Richard Ellis, Sharadah Essapen, Aman-deep S Dhadha, Mark Harrison, Stephen Falk, Sherif Raouf, Charlotte Rees, Rene K Olesen, David Propper, John Bridgewater, Ashraf Azzabi, David Farrugia, Andrew Webb, David Cunningham, Tamas Hickish, Andrew Weaver, Simon Gollins, Harpreet S Wasan, and James Paul. 3 versus 6 months of adjuvant oxaliplatin-fluoropyrimidine combination therapy for colorectal cancer (SCOT): an international, randomised, phase 3, non-inferiority trial. *The Lancet Oncology*, 19(4):562–578, apr 2018. ISSN 14702045. doi:10.1016/S1470-2045(18)30093-7. URL <https://linkinghub.elsevier.com/retrieve/pii/S1470204518300937>.
- Ronan A. Battle, Anita M. Chandran, Timothy H. Runcorn, Arnaud Mussot, Alexandre Kudlinski, Robert T. Murray, and J. Roy Taylor. Mid-infrared difference-frequency generation directly pumped by a fiber four-wave mixing source. *Optics Letters*, 48(2):387, jan 2023. ISSN 0146-9592. doi:10.1364/OL.476754. URL <https://opg.optica.org/abstract.cfm?URI=ol-48-2-387>.
- Jing Liu, Zongliang Gan, and Xiuchang Zhu. Directional Bicubic Interpolation — A New Method of Image Super-Resolution. 2013. doi:10.2991/icmt-13.2013.57. URL <https://www.atlantis-press.com/article/10409>.
- Rolf Theodor Borlinghaus and Constantin Kappel. HyVolution—the smart path to confocal super-resolution. *Nature Methods*, 13(3):i–iii, 2016. ISSN 1548-7091. doi:10.1038/nmeth.f.392.
- Jun Li, Alexander Agathos, Daniela Zaharie, José M. Bioucas-Dias, Antonio Plaza, and Xia Li. Minimum volume simplex analysis: A fast algorithm for linear hyperspectral unmixing. *IEEE Transactions on Geoscience and Remote Sensing*, 53(9):5067–5082, 2015. ISSN 01962892. doi:10.1109/TGRS.2015.2417162.
- Akshay Iyer, Anouk A.J. Hamers, and Asha B. Pillai. CyTOF® for the Masses. *Frontiers in Immunology*, 13(April): 14–17, 2022. ISSN 16643224. doi:10.3389/fimmu.2022.815828.
- Arun Satelli and Shulin Li. Vimentin in cancer and its potential as a molecular target for cancer therapy. *Cellular and Molecular Life Sciences*, 68(18):3033–3046, sep 2011. ISSN 1420-682X. doi:10.1007/s00018-011-0735-1. URL <http://link.springer.com/10.1007/s00018-011-0735-1>.
- Michael E. Tipping and Christopher M. Bishop. Bayesian image super-resolution. *Advances in Neural Information Processing Systems*, 2003. ISSN 10495258.
- Jocelyn Tillner, Vincen Wu, Emrys A. Jones, Steven D. Pringle, Tamas Karancsi, Andreas Dannhorn, Kirill Veselkov, James S. McKenzie, and Zoltan Takats. Faster, More Reproducible DESI-MS for Biological Tissue Imaging. *Journal of the American Society for Mass Spectrometry*, 28(10):2090–2098, 2017. ISSN 18791123. doi:10.1007/s13361-017-1714-z.

- Sami Koho, Giorgio Tortarolo, Marco Castello, Takahiro Deguchi, Alberto Diaspro, and Giuseppe Vicidomini. Fourier ring correlation simplifies image restoration in fluorescence microscopy. *Nature Communications*, 10(1), 2019. ISSN 20411723. doi:10.1038/s41467-019-11024-z.
- Alain Hore and Djemel Ziou. Image Quality Metrics: PSNR vs. SSIM. In *2010 20th International Conference on Pattern Recognition*, pages 2366–2369. IEEE, aug 2010. ISBN 978-1-4244-7542-1. doi:10.1109/ICPR.2010.579. URL <http://ieeexplore.ieee.org/document/5596999/>.
- A. Mittal, A. K. Moorthy, and A. C. Bovik. No-Reference Image Quality Assessment in the Spatial Domain. *IEEE Transactions on Image Processing*, 21(12):4695–4708, dec 2012. ISSN 1057-7149. doi:10.1109/TIP.2012.2214050. URL <http://ieeexplore.ieee.org/document/6272356/>.
- N. Venkatanath, D. Praneeth, B. H. Maruthi Chandrasekhar, Sumohana S. Channappayya, and Swarup S. Medasani. Blind image quality evaluation using perception based features. *2015 21st National Conference on Communications, NCC 2015*, 2015. doi:10.1109/NCC.2015.7084843.
- Raimund J. Ober, Sripad Ram, and E. Sally Ward. Localization Accuracy in Single-Molecule Microscopy. *Biophysical Journal*, 86(2):1185–1200, 2004. ISSN 00063495. doi:10.1016/S0006-3495(04)74193-4. URL [http://dx.doi.org/10.1016/S0006-3495\(04\)74193-4](http://dx.doi.org/10.1016/S0006-3495(04)74193-4).
- Lawrence Mosley. *A balanced approach to the multi-class imbalance problem*. PhD thesis, Iowa State University, Digital Repository, Ames, 2013. URL <https://lib.dr.iastate.edu/etd/13537/>.